Monthly Notices
of the
ROYAL ASTRONOMICAL SOCIETY

MNRAS **469,** 2821–2833 (2017)
Advance Access publication 2017 May 25

doi:10.1093/mnras/stx949

The Python Sky Model: software for simulating the Galactic microwave sky

B. Thorne,* J. Dunkley, D. Alonso and S. Næss
Department of Physics, University of Oxford, Keble Road, Oxford OX1 3RH, UK

Accepted 2017 April 19. Received 2017 April 12; in original form 2016 August 9

ABSTRACT

We present a numerical code to simulate maps of Galactic emission in intensity and polarization at microwave frequencies, aiding in the design of cosmic microwave background experiments. This PYTHON code builds on existing efforts to simulate the sky by providing an easy-to-use interface and is based on publicly available data from the *WMAP* (*Wilkinson Microwave Anisotropy Probe*) and *Planck* satellite missions. We simulate synchrotron, thermal dust, free–free and anomalous microwave emission over the whole sky, in addition to the cosmic microwave background, and include a set of alternative prescriptions for the frequency dependence of each component, for example, polarized dust with multiple temperatures and a decorrelation of the signals with frequency, which introduce complexity that is consistent with current data. We also present a new prescription for adding small-scale realizations of these components at resolutions greater than current all-sky measurements. The usefulness of the code is demonstrated by forecasting the impact of varying foreground complexity on the recovered tensor-to-scalar ratio for the LiteBIRD satellite. The code is available at: https://github.com/bthorne93/PySM_public.

Key words: cosmic background radiation – cosmology: observations.

1 INTRODUCTION

In recent years, the temperature and polarization anisotropies of the cosmic microwave background (CMB) have been measured with increasing precision by the *Wilkinson Microwave Anisotropy Probe* (*WMAP*) and *Planck* satellites (Hinshaw et al. 2013; Planck Collaboration I 2016a), coupled with ground- and balloon-based observations. The constraints these observations place on the parameters that describe the cosmology of the Universe have been tight enough to usher in the era of 'precision cosmology'.

Further progress will be made by measuring the polarization anisotropies of the CMB to greater precision. It is in the power spectrum of these anisotropies that the signature of primordial gravitational waves may be found, which would provide strong evidence in support of the scenario that the Universe went through an early period of inflation (e.g. Baumann et al. 2009). Current polarization data are starting to provide the strongest constraints on primordial gravitational waves (BICEP2/Keck Collaboration et al. 2015).

The CMB temperature anisotropy dominates over foreground emission from the Galaxy in a broad range of frequencies. In contrast, the polarized CMB signal is weaker than the strongly polarized Galactic thermal dust and synchrotron radiation. In particular, the divergence-free *B*-mode polarization signal sourced by primordial gravitational waves at recombination is predicted to be at least several orders of magnitude weaker than the polarized foregrounds, averaged over the sky, and is a subdominant signal even in the cleanest sky regions (Planck Collaboration XXII 2015).

To optimize our ability to extract the CMB polarization signal from upcoming and future experiments, we rely on realistic models of the Galactic emission to simulate observations of these components at a range of frequencies. Several sky simulation tools are already publicly available, including the Planck Sky Model (Delabrouille et al. 2013) and the Global Sky Model (de Oliveira-Costa et al. 2008; Zheng et al. 2017). While our work was in preparation, a similar modelling and software effort was presented in Hervías-Caimapo, Bonaldi & Brown (2016) for polarized Galactic emission.

With the new code presented here, we build on existing efforts, providing a flexible and easily used tool for simulating Galactic emission that includes recent public data from the *Planck* satellite. Unique to this code, we define a set of viable alternative models that are consistent with current data, in combination with a new prescription to simulate smaller scale realizations of the components. We do not attempt to physically model the emission in three dimensions via, for example, integrating a dust or electron density over a Galactic magnetic field (e.g. Waelkens et al. 2009; Fauvet et al. 2011; Fauvet, Macías-Pérez & Désert 2012; Jansson & Farrar 2012; Orlando & Strong 2013; Beck et al. 2016). Instead, we adopt empirical models that describe the frequency scaling of each component with simple forms consistent with current data, using high signal-to-noise ratio maps of each component as templates at

* E-mail: ben.thorne@physics.ox.ac.uk

© 2017 The Authors
Published by Oxford University Press on behalf of the Royal Astronomical Society

Downloaded from https://academic.oup.com/mnras/article/469/3/2821/3752444 by Princeton University user on 16 July 2024

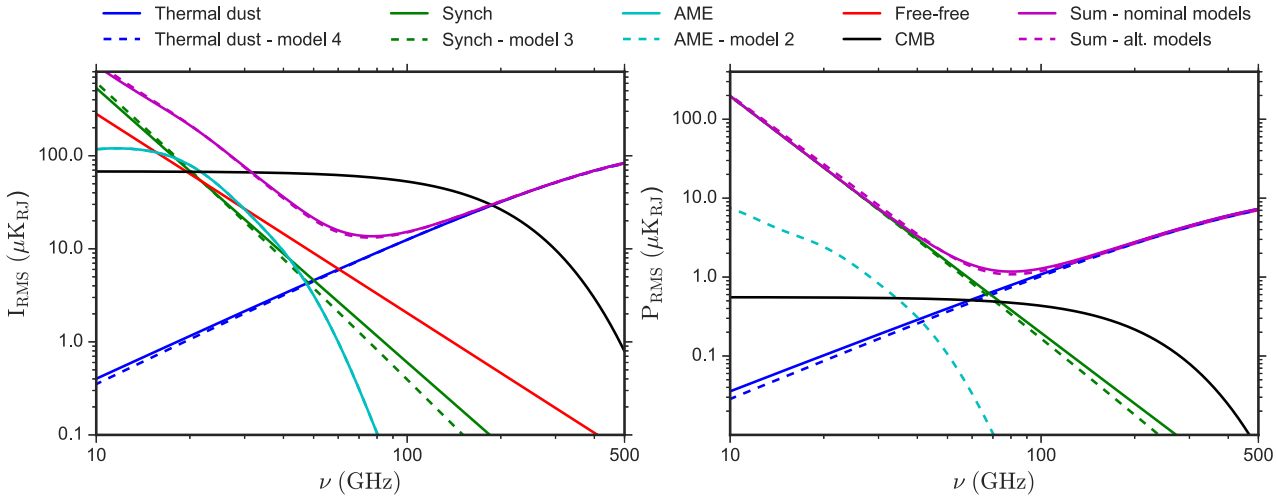

Figure 1. The frequency scaling laws for the individual components of PYSM; we show the nominal and alternative models as solid and dashed lines, respectively. We show only the alternative models that have a significant impact on the shape of the spectrum. These spectra are calculated by producing masked maps of each component at each frequency, smoothing to FWHM 1° in intensity and 40 arcmin in polarization, and then computing the rms. The mask used in intensity is the *WMAP* 9-yr KQ85 mask, and the polarization mask is the *Planck* polarization confidence mask CPM83.

frequencies far from the foreground minimum. These simulations will not therefore capture all the complexity present in the true emission.

The structure of this paper is as follows: In Section 2, we describe the structure of the code together with the models and alternatives used for each component. In Section 3, we describe a procedure to add small-scale anisotropy to the simulated maps. In Section 4, we describe a method used to introduce a decorrelation of the signal in each component as a function of frequency; and in Section 5, we demonstrate the usefulness of these simulations by forecasting the impact of foreground complexity on the uncertainty of the recovered tensor-to-scalar ratio for the LiteBIRD experiment as an example.

2 LARGE-SCALE SIMULATIONS

We simulate Galactic diffuse emission in intensity and polarization from four Galactic components: thermal dust, synchrotron, free–free and anomalous microwave emission (AME). We also include a gravitationally lensed CMB realization and white instrument noise. Maps can be integrated over a top-hat bandpass, describing the response of each experimental channel, and smoothed with a Gaussian beam.

The user specifies a set of observation frequencies, beam widths, bandpass widths, noise and chosen output components and units. The code simulates each component at each frequency using a phenomenological model. One or more emission template maps are defined at pivot frequencies, and then the extrapolation in frequency is performed using scaling laws and maps of spectral parameters. A lensed CMB realization can be included by calling the TAYLENS software (Næss & Louis 2013) directly, or using a pre-calculated realization.

In this section, we describe the suite of models available in PYSM (Python Sky Model). These models are designed to cover a range of new complexities found to be consistent with the most recent *WMAP* and *Planck* data. For example, we provide a new model of synchrotron spectral index steepening consistent with *WMAP* 9-yr data, and a model of dust decorrelation with frequency, an effect detected in the most recent *Planck* analysis (Planck Collaboration et al. 2017) and compatible with spatially varying spectral indices. Careful consideration of such effects is vital in the design of the next generation of CMB experiments seeking to constrain the tensor-to-scalar ratio in order to avoid bias introduced by model mismatch. Furthermore, we provide for the first time simulations of small-scale power modulated by the signal-dominated large-scale power, making these maps suitable for both full sky analysis and the analysis of small patches in high-Galactic-latitude regions.

The intensity and polarized emission as a function of frequency for the models we consider are summarized in Fig. 1, together with the template maps in Fig. 2.

2.1 Synchrotron

Synchrotron radiation is the dominant radiation mechanism in polarization at frequencies $\lesssim$50 GHz (e.g. Kogut et al. 2007). It is produced by cosmic rays spiralling around Galactic magnetic fields and radiating. The power and spectral energy distribution (SED) depend on both the strength of the local magnetic field and the energy distribution of the injected cosmic rays. The polarization of the radiation depends on the orientation of the intervening magnetic field. The predicted dependence of the spectrum on the magnetic field for a population of cosmic rays with energy distribution $N(E) \propto E^{-p}$ is, in antenna temperature units:

$$I_\nu \propto B^{\frac{p+1}{2}} \nu^\beta, \tag{1}$$

where $\beta = -\frac{(p+3)}{2}$ (Rybicki & Lightman 1979). The spectral index, β, is expected to have some spatial variability and to vary with frequency. As synchrotron sources age, their SED steepens, since high-frequency radiation corresponds to higher energy particles that radiate energy away most rapidly. Along a line of sight, there will likely also be multiple synchrotron components, and the stacking of their spectra can lead to flattening of the SED. The spectrum can also be flattened through effects of synchrotron self-absorption, which tends to be more significant towards the Galactic Centre.

2.1.1 *Model 1: nominal index*

The nominal PYSM model assumes that the synchrotron intensity is a scaling of the degree-scale-smoothed 408-MHz Haslam map

Downloaded from https://academic.oup.com/mnras/article/469/3/2821/3752444 by Princeton University user on 16 July 2024

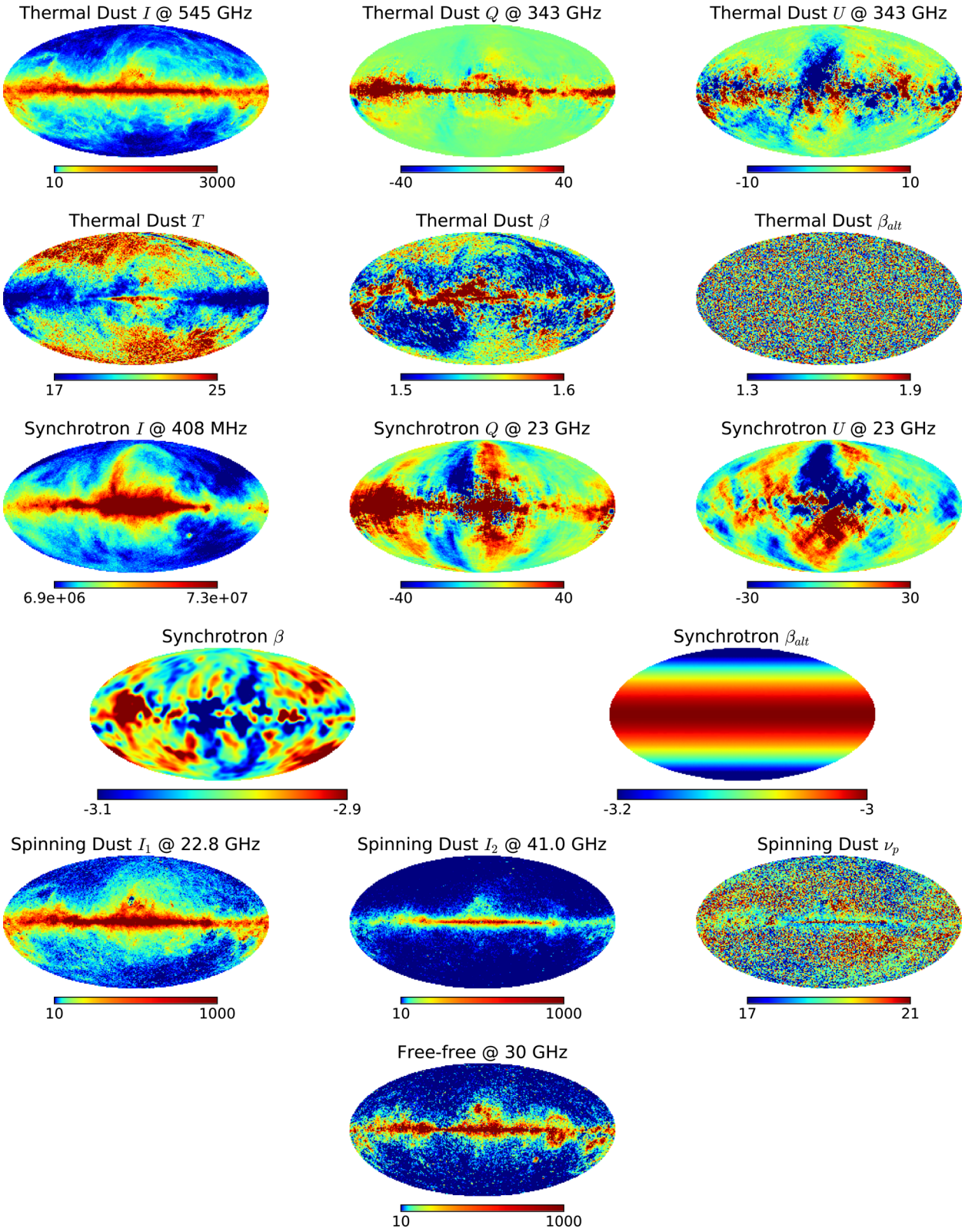

Figure 2. Template maps used in the PYSM models. All emission templates are in units of μK_{RJ} and all dust temperature templates are in units of K. Intensity templates are plotted on a log scale, and the polarization templates are plotted on a linear scale.

Downloaded from https://academic.oup.com/mnras/article/469/3/2821/3752444 by Princeton University user on 16 July 2024

(Haslam et al. 1981; Haslam et al. 1982), reprocessed by Remazeilles et al. (2015). It models the polarization as a scaling of the *WMAP* 9-yr 23-GHz Q and U maps (Bennett et al. 2013), smoothed to 3°. Both of these maps have small scales added using the prescription described in Section 3.

In the nominal model, we simulate the spectral index as being a power law in every direction, such that

$$I_\nu^{\rm Synch}(\hat{\boldsymbol{n}}) = A_{\nu_0}(\hat{\boldsymbol{n}}) \left(\frac{\nu}{\nu_0}\right)^{\beta_{\rm s}(\hat{\boldsymbol{n}})}. \quad (2)$$

As in the nominal Planck Sky Model v1.7.8 simulations, we use the spectral index map from 'Model 4' of Miville-Deschenes et al. (2008), calculated from a combination of Haslam and *WMAP* 23-GHz polarization data using a model of the Galactic magnetic field. We assume that the index is the same in temperature and polarization, although the true sky will most likely be more complicated than this. The template maps and index map are shown in Fig. 2.

2.1.2 Model 2: spatially steepening index

The cosmic rays responsible for synchrotron radiation are thought to be energized by processes such as supernovae, which are more common in the Galactic plane. Synchrotron emission observed at higher latitudes will therefore likely be produced by older cosmic rays that have diffused out of the Galactic plane and therefore lost more energy. This is expected to result in the steepening of the synchrotron spectral index away from the plane (Kogut 2012; Ichiki 2014). Evidence for steepening in the polarization emission has been seen in Kogut et al. (2007), Fuskeland et al. (2014) and Ruud et al. (2015) using *WMAP* and QUIET data.

We parametrize the steepening with a smoothly varying index described by a gradient δ_β that scales with Galactic latitude, b, such that $\beta_{\rm s} = \beta_{\rm s,b=0} + \delta_\beta \sin|b|$. In Model 2, we use $\delta_\beta = -0.3$, consistent with *WMAP* polarization data (Kogut et al. 2007; Hinshaw et al. 2013). The simulated index varies from $\beta_{\rm s} = -3.0$ at the equator to $\beta_{\rm s} = -3.3$ at the poles in both intensity and polarization, as shown in Fig. 2.

2.1.3 Model 3: curvature of index

The synchrotron emission may be better modelled by a curved spectrum that either flattens or steepens with frequency. Model 3 simulates the steepening or flattening of the spectral index above a frequency, ν_c, as

$$I_\nu^{\rm Synch}(\hat{\boldsymbol{n}}) = A_{\nu_0}(\hat{\boldsymbol{n}}) \left(\frac{\nu}{\nu_0}\right)^{\beta_{\rm s}(\hat{\boldsymbol{n}})+C\ln(\frac{\nu}{\nu_c})}, \quad (3)$$

where positive C corresponds to flattening and negative C to steepening.

Kogut (2012) fits this model to a small patch of sky with 10 overlapping radio frequency sky surveys and *WMAP* 23-GHz data, finding best-fitting values of $\beta = -2.64 \pm 0.03$ and $C = -0.052 \pm 0.005$ at 0.31 GHz. This corresponds to a steepening of about 0.57 between 408 MHz and 94 GHz. Evaluating the spectral index at 23 GHz, Kogut (2012) finds $\beta_{23} = -3.09 \pm 0.05$. This is consistent with the index map in model 1 that has a mean and standard deviation of -3.00 ± 0.06. Therefore, for simplicity, we use the same map as model 1 from Miville-Deschenes et al. (2008) for $\beta(\hat{\boldsymbol{n}})$, and a baseline curvature value of $C = -0.052$ at $\nu_c = 23$ GHz.

2.2 Thermal dust emission

At frequencies greater than ≈70 GHz, the polarized foreground spectrum is dominated by thermal dust emission. The dust grains are thought to be a combination of carbonaceous and silicate grains, and polycyclic aromatic hydrocarbons (PAHs). The total emission results from the interaction of these species with the interstellar radiation field: The grains are heated by absorption in the optical and cooled by emitting in the far-infrared (FIR; e.g. Draine 2011). The thermal dust is polarized since aspherical dust grains preferentially emit along their longest axis, which tend to align perpendicular to magnetic fields.

In the frequency range of interest for CMB experiments, the spectrum is well approximated by a modified blackbody with a power-law emissivity, such that

$$I = A\nu^{\beta_{\rm d}} B_\nu(T_{\rm d}), \quad (4)$$

for spectral index $\beta_{\rm d}$ and temperature $T_{\rm d}$, where B_ν is the Planck function. A single component at $T = 15.9$ K fits the *Planck* data well (Planck Collaboration X 2016b), with different indices preferred by the intensity ($\beta = 1.51 \pm 0.01$) and polarization (1.59 ± 0.02) data. This difference indicates the presence of multiple components with different polarization properties.

In intensity, the two-component model of Finkbeiner, Davis & Schlegel (1999), with a hot and cold component at 9.4 and 16 K, is marginally preferred (Meisner & Finkbeiner 2015). They use this model to extrapolate 100-μm emission and 100/240-μm flux ratio maps to microwave frequencies. The exact physical model is not well constrained by current observations, including the number of components, spatial variablility of spectral index and spatial variation of the dust temperature.

2.2.1 Model 1: nominal index

Our nominal model uses template maps at 545 GHz in intensity and 353 GHz in polarization. We use the templates estimated from the *Planck* data using the 'COMMANDER' code (Planck Collaboration X 2016b). In polarization, these maps closely match the 353-GHz *Planck* data, which are dominated by thermal dust. We use the $N_{\rm side}$ 2048 dust intensity maps degraded to $N_{\rm side}$ 512, and the polarization product smoothed to 2° FWHM (full width at half-maximum) in polarization with small-scale variations added by the procedure described in Section 3.

In the nominal simulations, we model the frequency scaling as a single component, using the best-fitting emissivity estimated by the COMMANDER fit. The emission model is given by

$$\begin{aligned} I_\nu^{\rm d}(\hat{\boldsymbol{n}}) &= A_{{\rm I},\nu_{\rm I}}(\hat{\boldsymbol{n}})(\nu/\nu_{\rm I})^{\beta_{\rm d}(\hat{\boldsymbol{n}})} B_\nu(T_{\rm d}(\hat{\boldsymbol{n}})), \\ \left\{Q_\nu^{\rm d}(\hat{\boldsymbol{n}}), U_\nu^{\rm d}(\hat{\boldsymbol{n}})\right\} &= \{A_{{\rm Q},\nu_{\rm P}}(\hat{\boldsymbol{n}}), A_{{\rm U},\nu_{\rm P}}(\hat{\boldsymbol{n}})\} \\ &\quad \times (\nu/\nu_{\rm P})^{\beta_{\rm d}(\hat{\boldsymbol{n}})} B_\nu(T_{\rm d}(\hat{\boldsymbol{n}})). \end{aligned} \quad (5)$$

Here $\nu_{\rm I} = 545$ and $\nu_{\rm P} = 353$ GHz. We assume that the intensity and polarization share the same index, as was assumed in the COMMANDER-fitting process. Both $\beta_{\rm d}$ and $T_{\rm d}$ vary spatially; the maps are shown in Fig. 2.

This model will not capture all of the physical complexity as it is likely that silicate and carbonaceous grains have distinct emissivities. They also likely have different degrees of polarization, since the efficiency of the grain alignment varies with the size and shape of grain. This would result in the polarization fraction in dust being a function of frequency, with some evidence for this shown in Planck Collaboration XXII (2015).

Downloaded from https://academic.oup.com/mnras/article/469/3/2821/3752444 by Princeton University user on 16 July 2024

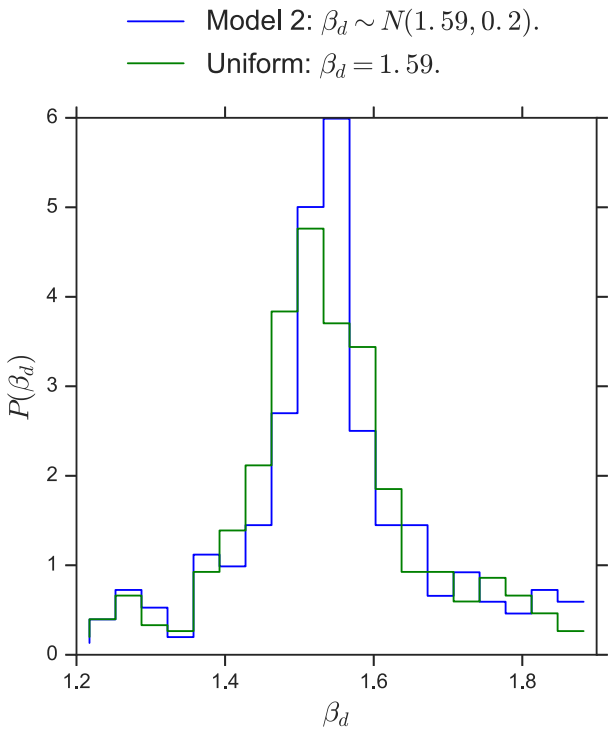

Figure 3. Normalized histograms of the dust spectral index, β_d, calculated for noisy simulations of different PYSM models with a varying intrinsic index dispersion. We see that the resulting dispersions are very similar, indicating noise-dominated data.

2.2.2 *Models 2 and 3: spatially variable index*

The dust index is expected to vary spatially, in particular, in polarization, but current data cannot strongly constrain this possible variation. We perform a test to assess how well a varying index can be detected by the *Planck* data, given the current noise levels.

We simulate a spectral index map with degree-scale variation drawn from a Gaussian of mean 1.59 and dispersion σ. We then simulate polarized dust emission in Stokes Q and U at 217 and 353 GHz at $N_{\rm side} = 128$ for σ in the range 0.05–0.7. We produce noise maps at 217 and 353 GHz using the *Planck* half-mission full-sky maps at 217 and 353 GHz. We first degrade these to $N_{\rm side}$ 128 and then, at each frequency, take the difference between the two half-mission maps and divide it by a factor of 2. Finally, we smooth each noise map with a Gaussian kernel of 1° FWHM. We then estimate the index from these maps in circles of radius 10° centred on HEALPIX $N_{\rm side} = 8$ pixels, using

$$\beta_{\rm d}(\hat{\boldsymbol{n}}) = \frac{\ln\left(\frac{[Q,U]_1(\hat{\boldsymbol{n}})}{[Q,U]_2(\hat{\boldsymbol{n}})}\frac{B(\nu_2, T(\hat{\boldsymbol{n}}))}{B(\nu_1, T(\hat{\boldsymbol{n}}))}\right)}{\ln\left(\frac{\nu_2}{\nu_1}\right)} + 2. \quad (6)$$

This follows a similar method used in the comparable *Planck* analysis in Planck Collaboration XXII (2015), except we neither use the 143-GHz channel and do not add CMB and synchrotron, nor fit for them. We use a similar region as the *Planck* analysis, shown in Fig. 4. The dispersion of the indices for a uniform input index of 1.59, and for an input index map with degree-scale variation of standard deviation of 0.2 is shown in Fig. 3, and can be compared to Fig. 9 in Planck Collaboration XXII (2015). The statistics of the recovered index distributions for these two models, the nominal model and a model with a larger standard deviation of 0.3 are shown in Table 1.

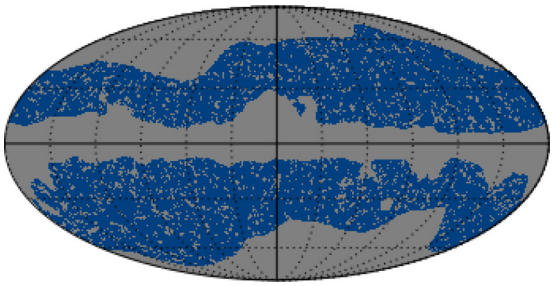

Figure 4. Mask used in calculation of $\beta_{\rm d}$ in Section 2.2.2. This mask is an approximation to the one used in the *Planck* analysis (fig. 1 of Planck Collaboration XXII 2015).

Table 1. Statistics of dust polarization index calculated from different simulations of dust polarization at 217 and 353 GHz containing instrumental noise compatible with the corresponding *Planck* channels.

Model	Mean	Standard deviation
Nominal	1.53	0.22
$\sigma(\beta) = 0.2$	1.58	0.24
$\sigma(\beta) = 0.3$	1.58	0.23
Uniform	1.58	0.23

The distributions for $\beta_{\rm d}$ are similar since the data are noise-dominated. The dispersion due to noise is ∼0.22 compared to the value of 0.17 found in Planck Collaboration XXII (2015), and the value of 0.22 found in a comparable calculation by Poh & Dodelson (2016). This indicates that models of the dust spectral index with significant spatial variation on degree scales are still consistent with the data. Furthermore, a recent analysis of decorrelation of the *Planck* half-mission and detector set maps found an intrinsic variation of 0.07 in the dust index (Planck Collaboration et al. 2017). Models 2 and 3 therefore modify the nominal dust model with a different spectral index map. The spectral index of model 2 (3) is a Gaussian random field with mean of 1.59 and $\sigma = 0.2(0.3)$ varying on degree scales for both intensity and polarization.

2.2.3 *Model 4: two dust temperatures*

One can also consider a number $N_{\rm d}$ of dust components with their own temperatures and spectral indices:

$$I(\hat{\boldsymbol{n}}, \nu) = \sum_{a=1}^{N_{\rm d}} I_a(\hat{\boldsymbol{n}}) \left(\frac{\nu}{\nu_*}\right)^{\beta_a} \frac{B_\nu(T_a(\hat{\boldsymbol{n}}))}{B_{\nu_*}(T_a(\hat{\boldsymbol{n}}))}, \quad (7)$$

and similarly for polarization. For our fourth dust model, we use $N_{\rm d} = 2$, using the best-fitting model templates estimated by Meisner & Finkbeiner (2015) from the *Planck* data, using the model from Finkbeiner et al. (1999).

The model as proposed in these references can be written as

$$I(\hat{\boldsymbol{n}}, \nu) = I_{\nu_0}(\hat{\boldsymbol{n}}) \frac{\sum_{a=1}^{2} f_a\, q_a \left(\frac{\nu}{\nu_0}\right)^{\beta_a} B_\nu(T_a(\hat{\boldsymbol{n}}))}{\sum_{b=1}^{2} f_b\, q_b\, B_{\nu_0}(T_b(\hat{\boldsymbol{n}}))}, \quad (8)$$

where I_{ν_0} is the intensity template at 100 μm ($\nu_0 = 3000$ GHz), β_k are constant spectral indices, T_k are spatially varying dust temperatures, q_k is the IR/optical ratio for each species, f_k is the fraction of power absorbed from the interstellar radiation field and

Downloaded from https://academic.oup.com/mnras/article/469/3/2821/3752444 by Princeton University user on 16 July 2024

emitted in the FIR by each component, and we have omitted the colour-correction factors. In order to adapt this to the model in equation (7), we generate the separate amplitude templates $I_a(\hat{\boldsymbol{n}})$, at $\nu_* = 545$ GHz in terms of I_{ν_0} and $T_k(\hat{\boldsymbol{n}})$ as

$$I_{\rm a}(\hat{\boldsymbol{n}}) = I_{\nu_0}(\hat{\boldsymbol{n}}) \frac{\left(\frac{\nu_*}{\nu_0}\right)^{\beta_a} f_a\, q_a\, B_{\nu_*}(T_a(\hat{\boldsymbol{n}}))}{\sum_{b=1}^{2} f_b\, q_b\, B_{\nu_0}(T_b(\hat{\boldsymbol{n}}))}. \quad (9)$$

In polarization, we construct the polarization simulations using the polarization angles and fractional polarization from the 353-GHz template maps in Model 1, such that

$$Q(\nu, \hat{\boldsymbol{n}}) = f_{\rm d}(\hat{\boldsymbol{n}}) I(\nu, \hat{\boldsymbol{n}}) \cos(2\gamma(\hat{\boldsymbol{n}})),$$
$$U(\nu, \hat{\boldsymbol{n}}) = f_{\rm d}(\hat{\boldsymbol{n}}) I(\nu, \hat{\boldsymbol{n}}) \sin(2\gamma(\hat{\boldsymbol{n}})). \quad (10)$$

where $f_{\rm d} = \sqrt{Q^2 + U^2}/I$ at 353 GHz in Model 1.

2.3 Anomalous microwave emission

AME refers to emission with a spectral distribution not well approximated by known foreground models. It has been detected in compact objects, and in the diffuse sky, with early measurements by de Oliveira-Costa et al. (1997) and Leitch et al. (1997). It is spatially correlated with dust, and primarily important in the 20–40 GHz range, with a variable peak frequency (Stevenson 2014).

A likely model for the emission is rapidly spinning dust grains. Draine & Lazarian (1998) explain the emission by a population of grains of size $<3 \times 10^{-7}$cm, with modest electric dipole moments. A candidate for these grains is PAHs that are detected in vibrational emission in the range 3−12μm. The theoretical SEDs for such spinning PAH grains have been successfully fit to AME observations (Hoang, Lazarian & Draine 2011), but recent analysis of the *Planck* data has cast some doubt on their nature (Hensley, Draine & Meisner 2016). A second candidate for AME is magnetic dipole radiation due to thermal fluctuations of magnetization in small silicate dust grains (Draine & Lazarian 1999).

2.3.1 Model 1: nominal unpolarized AME

We model the AME using the *Planck* templates derived from the COMMANDER parametric fit to the *Planck* data (Planck Collaboration X 2016b), using the COMMANDER model:

$$I_\nu^{\rm AME}(\hat{\boldsymbol{n}}) = A_{\nu_{0,1}}(\hat{\boldsymbol{n}}) \epsilon(\nu, \nu_{0,1}, \nu_{p,1}(\hat{\boldsymbol{n}}), \nu_{p0}) + A_{\nu_{0,2}}(\hat{\boldsymbol{n}}) \epsilon(\nu, \nu_{0.2}, \nu_{p,2}, \nu_{p_0}). \quad (11)$$

Here, the first component has a spatially varying emissivity and the second component has a spatially constant emissivity. Both these emissivity functions are calculated using SPDUST2 (Ali-Haimoud, Hirata & Dickinson 2009; Silsbee, Ali-Haïmoud & Hirata 2011), evaluated for a cold neutral medium and shifted in $\log(\nu) - \log(I)$ space. The two template maps are shown in Fig. 2. This nominal AME model is unpolarized.

2.3.2 Model 2: polarized AME

AME is not thought to be strongly polarized, and the polarization fraction has been constrained to be below 1–3 per cent in the range 23–41 GHz by observations of the Perseus molecular complex using *WMAP* 7-yr data (Dickinson, Peel & Vidal 2011). More recent observations of AME emission from the molecular complex W43 by the QUIJOTE experiment have placed a 0.39 per cent upper limit on its polarization fraction, which falls to 0.22 per cent when combined with *WMAP* data (Génova-Santos et al. 2017). Remazeilles et al. (2016) found that neglecting a 1 per cent level of polarized AME can bias the derived value of the tensor-to-scalar ratio by non-negligible amounts for satellite missions.

To construct a template, we use the dust polarization angles, $\gamma_{\rm d}$, calculated from the *Planck* COMMANDER 2015 thermal dust Q and U maps at 353 GHz. The AME polarization is then

$$Q_a = f_a I_\nu \cos(2\gamma_{353}),\ U_a = f_a I_\nu \sin(2\gamma_{353}). \quad (12)$$

In this model, we assign a global polarization fraction of 2 per cent; the fraction can also be easily changed by varying the f_a parameter.

2.4 Free–free

Free–free emission is caused by electrons scattering off ions in the interstellar medium (Rybicki & Lightman 1979). The frequency scaling is well approximated by a function of the electron temperature and emission measure (Draine 2011). This is very close to a power law of −2.14 at frequencies greater than 1 GHz, and flattens abruptly at lower frequencies (Planck Collaboration X 2016b).

Free–free has been measured in *WMAP* and *Planck* intensity data, and it should be unpolarized since the scattering is independent of direction. However, there are small effects at the edges of dense ionized clouds due to the non-zero quadrupole moment in the electron temperature, which can cause up to 10 per cent polarization (e.g. Fraisse et al. 2009). The net polarization over the sky is estimated to be below 1 per cent (Macellari et al. 2011).

The PYSM nominal model for free–free emission assumes that it is unpolarized, and uses the degree-scale-smoothed emission measure and effective electron temperature COMMANDER templates (Planck Collaboration X 2016b). We apply the analytic law presented in Draine (2011) to produce an intensity map at 30 GHz, which we then scale with a spatially constant power-law index. We choose this index to be −2.14 consistent with *WMAP* and *Planck* measurements for electrons at ∼8000 K (Bennett et al. 2013; Planck Collaboration X 2016b). This gives

$$I_\nu^{\rm ff}(\hat{\boldsymbol{n}}) = A_{\nu_0}^{\rm ff}(\hat{\boldsymbol{n}}) \left(\frac{\nu}{\nu_0}\right)^{-2.14}. \quad (13)$$

Different behaviour will be expected below ∼0.01 GHz, where the COMMANDER model flattens (Planck Collaboration X 2016b).

2.5 CMN

We use the TAYLENS code (Næss & Louis 2013) in PYSM to generate a lensed CMB realization. The input to TAYLENS is a set of C_ls (C_{TT}, C_{EE}, C_{BB}, C_{TE}, $C_{\phi\phi}$, $C_{T\phi}$, $C_{E\phi}$) that have been calculated using the CAMB numerical code (Lewis, Challinor & Lasenby 2000). The nominal model uses Λ cold dark matter cosmological parameters that best fit the *Planck* 2015 data. We incorporate the functions of Taylens into the PYSM code for portability, so some functionality is removed.[1] We scale the CMB emission between frequencies using the blackbody function.

The user can opt to either run TAYLENS during the simulation, or use a pre-computed temperature and polarization map supplied with the code or generated by the user. If using TAYLENS, the CMB map can also be artificially delensed, with the expected lensing signal suppressed by a chosen factor.

[1] The original code is available at: https://github.com/amaurea/taylens.

Downloaded from https://academic.oup.com/mnras/article/469/3/2821/3752444 by Princeton University user on 16 July 2024

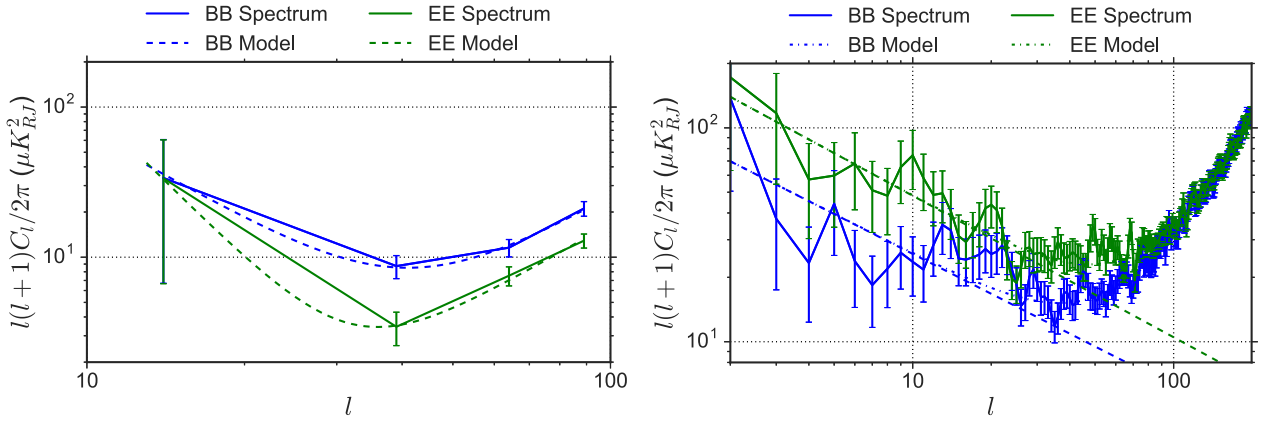

Figure 5. Left-hand panel: synchrotron polarization spectra in a square region centred on RA, Dec. = [0, −55] of size 1600 deg^2. The errors shown are cosmic variance only. The best-fitting power-law signal plus noise model from equation (15) is shown. The BB model minimum is used to estimate the scale l_* to smooth the maps. Right-hand panel: synchrotron polarization spectra computed with the *WMAP* polarization analysis mask, and best-fitting model. The dashed lines are the extrapolated power laws used in the small-scale simulation.

2.6 Instrument

We describe the instrument response with a simple top-hat bandpass, Gaussian white noise and Gaussian beam profile. The user specifies a central frequency, ν, and a width per band, $\Delta\nu$. The output signal is calculated using

$$I_{\nu,\Delta\nu}(\hat{\boldsymbol{n}}) = \int_{\nu-\frac{\Delta\nu}{2}}^{\nu+\frac{\Delta\nu}{2}} \frac{I_{\nu'}(\hat{\boldsymbol{n}})}{\Delta\nu} \mathrm{d}\nu'. \tag{14}$$

The white noise level is set per band for both intensity and polarization. The beam is characterized by an FWHM per channel. This instrument model will not capture realistic noise realizations or realistic bandpasses; the code is designed to be easily modifiable to incorporate such features.

3 SMALL-SCALE SIMULATIONS

Ground-based CMB experiments often observe only small patches of sky, and current data limit how well we can predict the small-scale behaviour of the foregrounds in high-latitude regions at the $\ell \sim 100$ scales of interest. Here, we describe our method for simulating sky maps at a higher resolution than the available data. Our approach is to extrapolate the angular power spectrum of the available data to smaller scales, drawing a Gaussian realization from this spectrum. Other similar methods have been implemented in Miville-Deschenes et al. (2008), Delabrouille et al. (2013), Remazeilles et al. (2015) and Hervías-Caimapo et al. (2016).

We simulate intensity and polarization maps using $M = M_0 + M_{\rm ss}$, where M_0 is the original smoothed data and $M_{\rm ss}$ is our small-scale simulation. We implement different methods in polarization and intensity for generating $M_{\rm ss}$. Although the real sky will be non-Gaussian, we limit these small-scale simulations to Gaussian or lognormal realizations.

3.1 Polarization

The *WMAP* and *Planck* polarization templates used in PYSM are all noise dominated at degree scales at high Galactic latitudes. To add power to the Q and U maps at small scales, we determine the multipole, ℓ_*, to which the original template is limited in resolution, smooth the maps to this scale, and add a realization of a model power-law spectrum to the smoothed templates. We compute angular power spectra on masked skies using the POLSPICE code[2] (Chon et al. 2004).

The scale ℓ_* varies spatially, but here we adopt a single global ℓ_*, which we determine by computing the polarization power spectra in a region centred on RA, Dec. = [0, −55], chosen as the location of the BICEP2/Keck patch. We choose a square region of side 40° for synchrotron, and 30° for dust, with a larger region for synchrotron as the maps are noisier. We fit the spectra with a signal-plus-noise model,

$$\frac{\ell(\ell+1)}{2\pi} C_\ell^{\rm BB} = A\ell^\gamma + N\frac{\ell(\ell+1)}{2\pi}, \tag{15}$$

approximating the uncertainties on the spectrum as due only to cosmic variance. The power-law model has previously been found to be an excellent fit to many observations of dust and synchrotron angular power spectra on large scales (e.g. Giardino et al. 2001; Planck Collaboration XXII 2015; Planck Collaboration et al. 2017). We choose to model the small-scale behaviour as an extension of this power law. We fit for three free parameters A, γ and N, and estimate ℓ_* as the scale at which this model is minimal in *BB* or *EE*. The masked synchrotron and dust *EE* and *BB* spectra are shown in Figs 5 and 6. We find $\ell_*^{\rm synch} = 36$ and $\ell_*^{\rm dust} = 69$.

We generate the large-scale templates, M_0, by smoothing the original maps with a Gaussian kernel of FWHM $\theta_{\rm fwhm} = 180/\ell_*{}^\circ$. We then construct $M_{\rm ss}$ by assuming that the small scales follow a power-law behaviour with $\frac{\ell(\ell+1)}{2\pi} C_\ell^{\rm XX} = A^{\rm XX}\ell^{\gamma^{\rm XX}}$. We find $A^{\rm XX}$ and γ^{XX} by fitting this model to the *EE* and *BB* spectra calculated on the original template with a Galactic mask. We use the *WMAP* polarization analysis mask for synchrotron (Gold et al. 2011), and the 80 per cent mask provided in the second *Planck* data, which we refer to here as Gal80. We find $\gamma^{\rm synch,EE} = -0.66$, $\gamma^{\rm synch,BB} = -0.62$, $\gamma^{\rm dust,EE} = -0.31$ and $\gamma^{\rm dust,BB} = -0.15$.

We multiply these power-law spectra by the window function $1 - W_\ell(\ell_*)$, where $W_\ell = \exp(-\sigma^2(\ell_*)\ell^2)$ with $\sigma = \theta_{\rm fwhm}/\sqrt{8\ln(2)}$, such that it can be added to the large-scale map that has been smoothed by the window function W_ℓ. We then draw a pair of Q and U Gaussian random fields, $\delta_{\rm G}$, from this spectrum using the HEALPIX[3] routine *synfast*.

[2] The POLSPICE code is available at: http://www2.iap.fr/users/hivon/software/PolSpice/.
[3] The HEALPIX code is available at: http://healpix.sourceforge.net.

Downloaded from https://academic.oup.com/mnras/article/469/3/2821/3752444 by Princeton University user on 16 July 2024

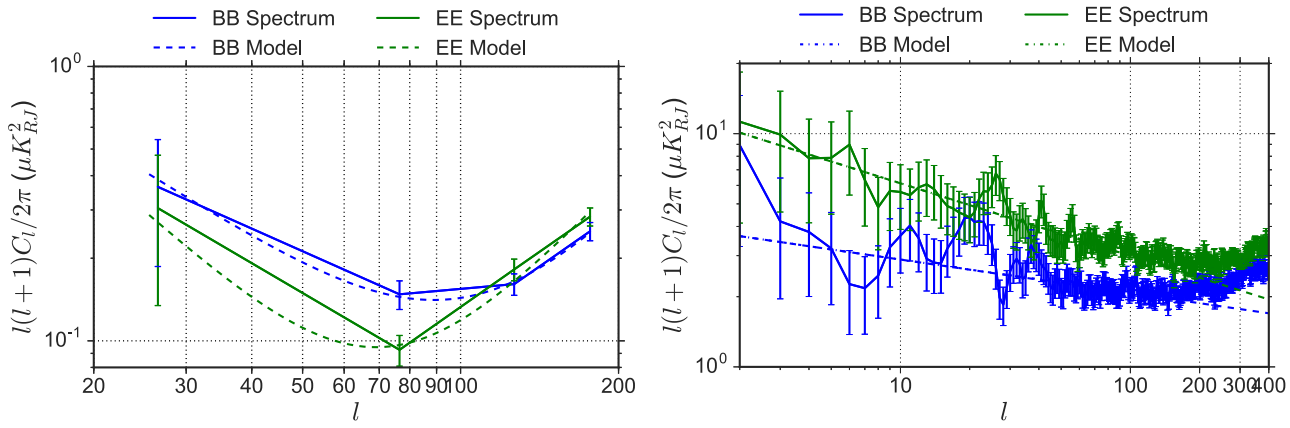

Figure 6. Left-hand panel: dust polarization spectra as in Fig. 5, but for a smaller patch of 800 deg^2. Right-hand panel: dust polarization spectra as in Fig. 5, but using the *Planck* Gal 80 Galactic plane mask.

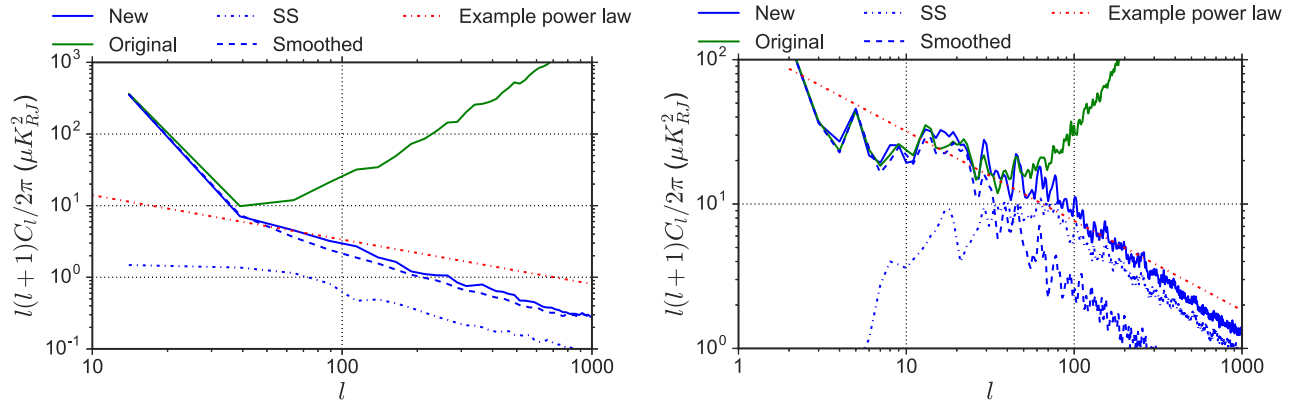

Figure 7. Left-hand panel: synchrotron *BB* spectra using the 1600 deg^2 region centred on RA, Dec. = [0, −55]. We show the original template, the smoothed template, the small-scale realization and the final map with small scales added. The dashed red line shows the shape of the power law of the small-scale realization to guide the eye. Right-hand panel: synchrotron *BB* spectra over 75 per cent of the sky using the *WMAP* polarization analysis mask.

We expect the true small-scale power to be modulated by the large-scale power, so we multiply the Gaussian random field by a spatially varying normalization such that

$$M_{\rm SS} = N(\hat{\boldsymbol{n}})\delta_{\rm G}(\hat{\boldsymbol{n}}). \tag{16}$$

We choose $N(\hat{\boldsymbol{n}})$ by dividing the sky into HEALPIX $N_{\rm side} = 2$ pixels and computing the angular power spectrum in each patch, $C_\ell(\hat{\boldsymbol{n}})$, and smoothing this map with FWHM 10° to avoid sharp pixel boundaries. We define

$$N(\hat{\boldsymbol{n}}) = \sqrt{\frac{C_{l_*}(\hat{\boldsymbol{n}})}{A\ell_*^\gamma}}, \tag{17}$$

so that the small-scale realization is normalized by the large-scale power in each patch. The $N(\hat{\boldsymbol{n}})$ for the dust Q template is shown in Fig. 9.

A patch of the resulting Q map for dust is shown in Fig. 10, illustrating the large-scale and additional small-scale components. We also show the power spectra of the maps in Figs 7 and 8, both for the masked all-sky maps and the smaller regions centred at [0,−55]. In both regions, the power-law behaviour is continuous at $\ell = \ell_*$.

We note that a limitation of this method is that it does not capture spatial variations in the modulation of the small-scale signal on scales smaller than $N_{\rm side}$ 2 pixels, so the normalization will not be accurate in these small regions.

3.2 Intensity: synchrotron

We use a similar procedure for simulating the intensity at small scales, but we use a lognormal rather than Gaussian distribution because it guarantees that the final map will be positive. It is also possible to generate a lognormal distribution from a Gaussian random field, and maintain the shape of the Gaussian field's angular power spectrum to a good approximation. In these simulations, we do not impose a correlation between the intensity and polarization at small scales.

For synchrotron, the Haslam template is provided at 57-arcmin resolution, which defines M_0. As for the polarization, we fit a power law to the signal, finding $\gamma = -0.55$. We draw a Gaussian realization $\delta_{\rm G}$ with variance $\sigma_{\rm G}^2$, but here we generate $M_{\rm ss}$ using a lognormal distribution with

$$M_{\rm ss} = M_0^{\rm min}\left[\exp\left(R(\hat{\boldsymbol{n}})\delta_{\rm G}(\hat{\boldsymbol{n}}) - \sigma_{\rm G}^2/2\right) - 1\right], \tag{18}$$

motivated by the requirement that intensity should be positive, a form commonly used in large-scale structure simulations (e.g. Kayo, Taruya & Suto 2001). Here, $R(\hat{\boldsymbol{n}})$ normalizes the small scales. Instead of using the local power spectrum, we normalize the small-scale intensity map by the large-scale intensity smoothed to 4° and raised to a power

$$R(\hat{\boldsymbol{n}}) = \left[\frac{M_0(\hat{\boldsymbol{n}})}{\langle M_0\rangle}\right]^\alpha.$$

Downloaded from https://academic.oup.com/mnras/article/469/3/2821/3752444 by Princeton University user on 16 July 2024

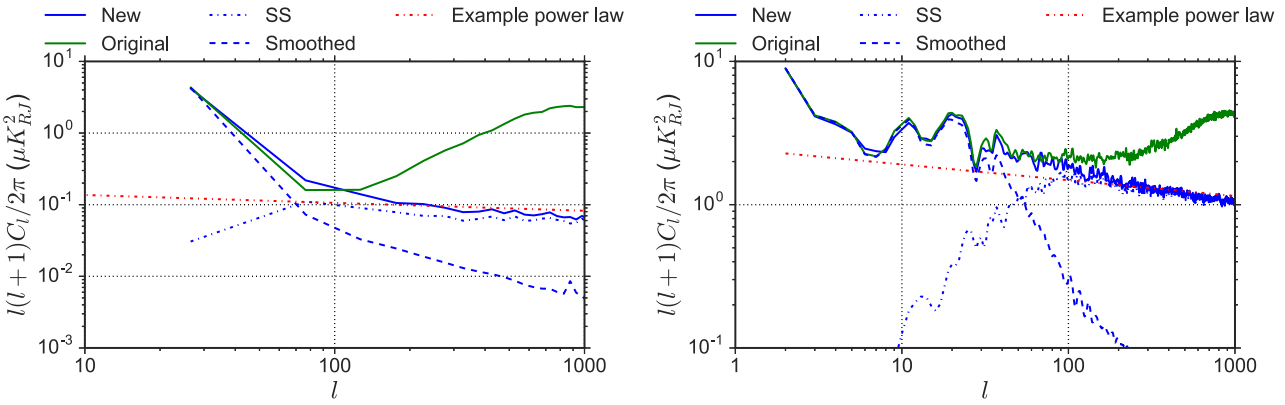

Figure 8. Left-hand panel: dust BB spectra in the 825 deg^2 region centred on RA, Dec. = [0, −55], as in Fig. 7. Right-hand panel: dust *BB* spectra in the Gal 80 region, as in Fig. 7.

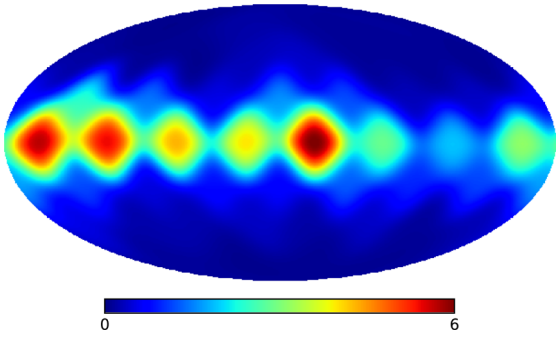

Figure 9. Normalization map, $N(\hat{\boldsymbol{n}})$, for the dust Q map.

We find the best-fitting $\alpha = 0.6$ that results in a total power spectrum of $\ell(\ell+1)C_\ell \propto \ell^\gamma$, fitted in the multipole range $200 < \ell < 1000$. An example of the synchrotron maps is shown in Fig. 11.

3.3 Intensity: free–free

The free–free template is smoothed at degree scales, which defines M_0. We found the lognormal procedure to be unsuitable for generating small scales for the free–free maps, as the comparatively larger dynamic range in small patches caused the exponential term to yield unrealistically large variation on small scales. We also found the free–free angular spectrum to be flatter than the synchrotron, so a direct extrapolation of the power law to smaller scales produced excess power at small scales, which is likely not physical. We therefore fixed the gradient of the free–free power spectrum to be $\gamma = -0.5$, and used this to generate a $\delta_{\rm G}$ realization with variance $\sigma_{\rm G}^2$. We then take the small-scale map to be

$$M_{\rm ss}(\hat{\boldsymbol{n}}) = R(\hat{\boldsymbol{n}})\delta_{\rm G}(\hat{\boldsymbol{n}}), \tag{19}$$

where $R(\hat{\boldsymbol{n}}) = \langle M_0\rangle(M_0(\hat{\boldsymbol{n}})/\langle M_0\rangle)^\alpha/4\sigma_{\rm G}$. We find that $\alpha = 1.15$ is the best-fitting value to recover the correct power-law behaviour of the power spectrum in the range $200 < \ell < 1000$. We redrew $\delta_{\rm G}$ for any negative pixels from additional full-sky realizations until we have positive values everywhere. This was necessary for <0.5 per cent of pixels. An example is shown in Fig. 11.

3.4 Intensity: thermal dust and AME

The *Planck* thermal dust map has a power spectrum in the low-foreground [RA, Dec. = 0, −55] region that falls off approximately as a power law. This indicates that the thermal dust intensity map is signal dominated in this high-Galactic-latitude region at small scales, and we do not add additional components.

The AME templates are limited to degree resolution, so we use the high-resolution thermal dust product as a proxy for the AME small scales. We produce the final AME map by multiplying the two intensity templates by the ratio of the high-resolution thermal dust template and the dust template smoothed to 1° FWHM. An example is shown in Fig. 11. The resulting AME templates therefore have the same small-scale morphology as the thermal dust template. Since the AME polarization templates are produced from the thermal dust polarization products, we do not simulate AME polarization separately.

4 FREQUENCY DECORRELATION

The spatial variation of spectral parameters discussed in Section 2 reflects the stochastic distribution of dust clouds and of the turbulent component of the magnetic field in the Galaxy. This spatial variability will realistically occur both across the sky and along the line of sight, and it will produce a frequency decorrelation that manifests as a departure from simple emission laws (Tegmark 1998; Santos, Cooray & Knox 2005). We implement this possible frequency decorrelation in PYSM using two different models.

4.1 Multiple components

For each component type described in Section 2, PYSM supports the inclusion of an arbitrary number of components with different amplitude and spectral index maps. This mimics the superposition of emission laws caused by the variation of spectral parameters along the line of sight.

4.2 Stochastic decorrelation

Let $m_\nu(\hat{\boldsymbol{n}}) = v_\nu(\hat{\boldsymbol{n}})f_\nu(\beta)$ be the sky emission of a given component as a function of frequency, where f_ν is any of the emission laws described in Section 2, governed by a set of spectral parameters β. The component v_ν is therefore the sky emission normalized by the emission law, so $v_\nu = v_{\nu'}$ in the absence of frequency decorrelation. In what follows, we write the harmonic coefficients of v_ν as a vector $\boldsymbol{v}$ of N_ν components, where N_ν is the total number of frequencies for each multipole (ℓ, m).

Downloaded from https://academic.oup.com/mnras/article/469/3/2821/3752444 by Princeton University user on 16 July 2024

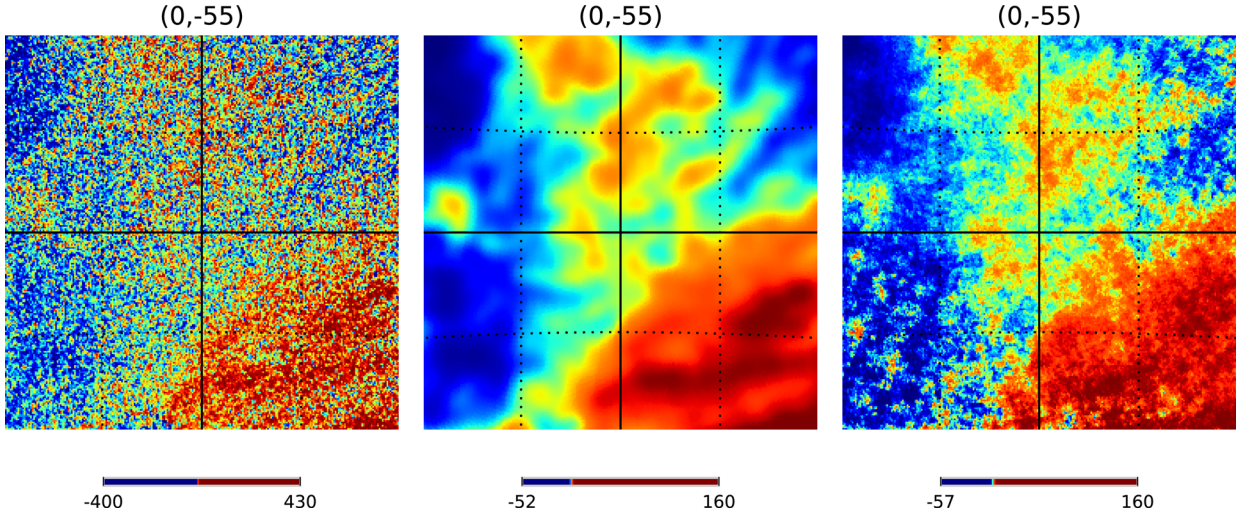

Figure 10. Gnomic projection of dust Q maps in a patch centred at RA, Dec. = (0, −55), 40° to a side. The left-hand panel is the original map, the middle panel has been smoothed (M_0) and the right-hand panel has had small scales added ($M_0 + M_{ss}$). The maps are plotted in histogram-equalization in units of μK_{RJ}.

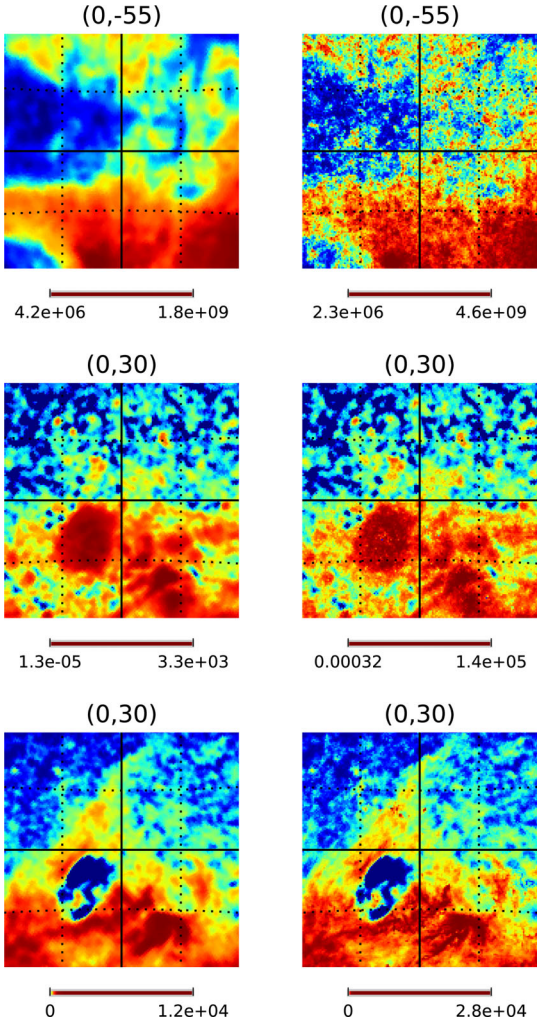

Figure 11. Synchrotron (top panel), free–free (middle panel) and AME (bottom panel) simulated intensity maps in a patch of side 40° centred at RA, Dec. as indicated. Left-hand panel: original template; right-hand: simulation including small scales. These have been plotted in histogram-equalization to increase the dynamic range.

We assume that the covariance between different frequencies takes the form

$$R_{\nu\nu'} \equiv \langle v_\nu v^*_{\nu'} \rangle = \langle |v_\nu|^2 \rangle \exp\left[-\frac{1}{2} \left(\frac{\log(\nu/\nu')}{\xi} \right)^2 \right], \tag{20}$$

following Vansyngel et al. (2016), where ξ is the correlation length in frequency space. Let us now decompose $\boldsymbol{v}$ as $\boldsymbol{v} = (c_1, c_2, \ldots, c_{N_c}, u_1, u_2, \ldots, u_{N_u})$, where c_i are sky maps corresponding to N_c observed templates at different frequencies, and u_i correspond to the sky emission in $N_u = N_\nu - N_c$ unobserved bands. The goal is to generate the unconstrained maps $\boldsymbol{u}$ with the correct correlation properties, as in equation (20), subject to the N_c constraints of the observed sky maps $\boldsymbol{c}$.

We simplify the process by making two assumptions:

(i) $\boldsymbol{u}$ is a Gaussian random variable.
(ii) $\langle |v_\nu|^2 \rangle$ does not depend on ν (although it may depend on ℓ, m).

The solution is then to draw a sample map from a multivariate Gaussian distribution given by

$$\boldsymbol{u} \longleftarrow \mathcal{N}(\bar{\boldsymbol{u}}, \mathbf{C}_{uu}), \tag{21}$$

where the mean $\bar{\boldsymbol{u}}$ and covariance $\mathbf{C}_{uu}$ are given by

$$\mathbf{C}_{uu} = \left(\left(\mathbf{R}^{-1} \right)_{uu} \right)^{-1}, \quad \bar{\boldsymbol{u}} = \mathbf{C}_{uu} \cdot (\mathbf{R}^{-1})_{uc} \cdot \boldsymbol{c}. \tag{22}$$

Here, $\mathbf{R}$ is the frequency covariance matrix in equation 20 and the subindices uu and uc select the $\boldsymbol{u} - \boldsymbol{u}$ and $\boldsymbol{u} - \boldsymbol{c}$ elements of the corresponding matrix.

In the current version of PYSM, we simplify this process further by considering only one constrained template at a single frequency for each component ($N_c = 1$), and by assuming that the angular distribution of all components is fully deterministic, such that all maps in $\boldsymbol{u}$ are proportional to c_1. The solution for the unconstrained maps then takes the simplified form

$$\boldsymbol{u}(\hat{\boldsymbol{n}}) = \left[\left(\left(\mathbf{r}^{-1} \right)_{uu} \right)^{-1/2} \boldsymbol{x} + \left(\left(\mathbf{r}^{-1} \right)_{uu} \right)^{-1} \left(\mathbf{r}^{-1} \right)_{uc} \right] c_1(\hat{\boldsymbol{n}}), \tag{23}$$

Downloaded from https://academic.oup.com/mnras/article/469/3/2821/3752444 by Princeton University user on 16 July 2024

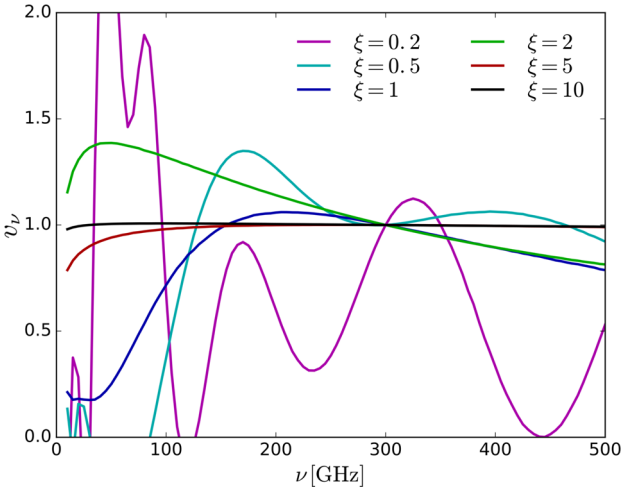

Figure 12. Examples of the frequency dependence of a given component for different correlation lengths ξ, normalized by the uncorrelated case, given a template at $\nu = 300$ GHz. The sharp kinks at low frequencies for small values of ξ are caused by the frequency correlation length being smaller than the sampling rate.

where $\boldsymbol{x}$ is an array of N_u Gaussian random numbers with unit variance and

$$r_{\nu\nu'} = \exp\left[-\frac{1}{2}\left(\frac{\log(\nu/\nu')}{\xi}\right)^2\right]. \quad (24)$$

It is worth noting that, for large correlation lengths, inverting $\mathbf{r}$ above is a numerically unstable operation. PYSM solves this by adding a small uncorrelated contribution to the diagonal of $\mathbf{r}$ only large enough to ensure that all of its eigenvalues are strictly positive. This ensures a stable matrix inverse while preserving the large-scale correlation structure. Fig. 12 shows examples of the corresponding emission laws for different values of ξ, normalized by the fully correlated case, for a template at $\nu = 300$ GHz. For comparison, ξ can be roughly related to the scatter in the spectral indices as $\xi \simeq \sigma_\beta^2$, and therefore a scatter of $\sigma_\beta \sim 0.2$ (see Section 2.2.2) would correspond to $\xi_{\rm dust} \sim 5$. Finally, the Gaussian model used to generate this stochastic decorrelation may cause the simulated fluctuations to take negative values for small correlation lengths and far away from the constrained frequencies. This is an undesirable feature, particularly in intensity (where positivity is a physical requirement), although it should not affect simulations with well-motivated correlation lengths (e.g. see above), assuming that the constrained frequencies are sufficiently close to the frequency range under study.

5 DISCUSSION

5.1 Forecast example

To illustrate the application of PYSM, we use it as a basis for forecasting the detectability of primordial tensor perturbations by a LiteBIRD-like satellite experiment (Matsumura et al. 2014). To do this, we generate simulated maps containing Galactic synchrotron (according to Model 1), thermal dust (according to Model 1) and CMB (with tensor-to-scalar ratio $r = 0$), and use the instrument specifications described in Table 2 to generate 100 different noise realizations.

We remove the foregrounds from each simulation using the Bayesian component separation algorithm described in Alonso et al. (2017), fitting for spatially varying spectral parameters (β_s, β_d, T_d) on HEALPIX pixels of size $N_{\rm side} = 16$, which corresponds to angular scales of $\sim 4^\circ$. Following Alonso et al. (2017), the foreground-cleaned maps are then used to generate a map of the expected variance after foreground removal by averaging over all simulations. Using the variance map, we generate CMB simulations with the appropriate noise levels, and then estimate the posterior distribution for r for each simulation using a simplified pixel-based likelihood (e.g. Hinshaw et al. 2007), marginalizing over the amplitude of lensing B-modes. Specifically, we fit for two parameters, r and $A_{\rm lens}$, that define the B-mode power spectrum as

$$C_\ell = r C_\ell^{\rm prim}(r = 1) + A_{\rm lens} C_\ell^{\rm B,lens}, \quad (25)$$

where $C_\ell^{\rm prim}$ and $C_\ell^{\rm B,lens}$ are templates for the primordial and lensing contributions to the B-mode power spectrum. All other parameters are kept fixed to the best-fitting values of Planck Collaboration XIII (2016c), except for the optical depth to reionization, which we fix to $\tau = 0.06$ in agreement with Planck Collaboration XLVI (2016d).

We compare the resulting posterior distribution for r with the one expected in the absence of foregrounds. This has a noise level of 4.5 μK arcmin in polarization co-added over frequency channels. The result for one of these simulations is shown in Fig. 13. We find that, in the ideal case of perfect knowledge of the foreground emission laws, a LiteBIRD-like experiment would be able to achieve a 1σ uncertainty of $\sigma(r) = 1.6 \times 10^{-4}$. We find that

Table 2. Specifications for LiteBIRD [taken from Matsumura et al. (2016)]. Note that noise levels are provided for polarization. All maps were smoothed to the lowest resolution of 70-arcmin FWHM, which does not correspond to the resolution achievable by LiteBIRD.

Frequency (GHz)	Noise rms (P) (μK arcmin)	FWHM (arcmin)
40, 50, 60	53.4, 32.3, 25.1	
68, 78, 89	19.6, 15.3, 12.4	
100, 119, 140	15.6, 12.6, 8.3	70
166, 195, 235	8.7, 6.7, 8.6	
280, 337, 402	19.0, 21.9, 52.3	

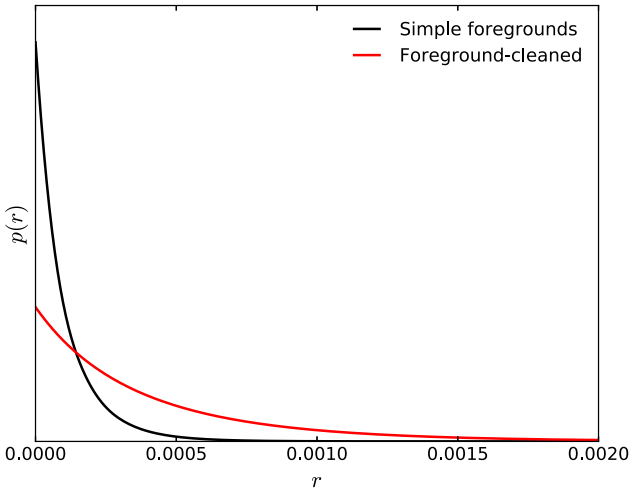

Figure 13. Forecasted posterior distribution for r estimated for one of the LiteBIRD-like simulations described in Section 5. The black line shows the results assuming perfect knowledge of the foreground spectral indices, while the red line corresponds to the case of spatially varying spectral indices on pixels of $N_{\rm side} = 16$, which more than doubles the uncertainty on r.

Downloaded from https://academic.oup.com/mnras/article/469/3/2821/3752444 by Princeton University user on 16 July 2024

this gets degraded after accounting for spatially varying spectral indices to $\sigma(r) = 3.7 \times 10^{-4}$, for the simulations considered in this example. This non-negligible inflation of errors demonstrates the importance of including realistic foreground levels in forecasts for future experiments.[4]

5.2 Conclusion

We have presented new software to simulate the Galactic microwave sky in polarization and intensity. The nominal models reflect the current understanding of Galactic foregrounds, and we have included a set of simple alternative models that capture physical extensions to these models and are still consistent with current data. There are many more possible alternatives that are not included, but we provide the public code in a way that makes adding further astrophysical complications straightforward. The code is also fast, portable, and easy to install and begin using.

We have developed methods for the addition of simulated small-scale variation in polarization and intensity, recovering power-law behaviour of the polarized components in sky patches of low and high signal, with minimal noise biasing. These simulations may aid in forecasting for ground-based observations limited to partial sky coverage. These small-scale simulations have certain limitations. Different simulated components are not correlated, and the small-scale procedure loses information in high signal-to-noise ratio regions by smoothing at a single scale. Incorporating the spatially varying signal-to-noise ratio into the definition of this smoothing scale would provide more accurate simulations. The small-scales will also be non-Gaussian in practice, which we do not account for.

There are other approaches to foreground modelling. PYSM uses two-dimensional (2D) sky maps and parametric models to extrapolate single-frequency maps to different frequencies, including the possibility of frequency decorrelation. This will be limited in its ability to replicate the polarized nature of Galactic foregrounds. Due to the combination of the complex three-dimensional structure of the Galaxy's magnetic field and the stacking of different sources along any given line of sight, we may expect the polarization fraction of any component to be a function of frequency. Even on a microphysical level, there is good evidence that the polarization spectrum of thermal dust is frequency-dependent (e.g. Planck Collaboration XXII 2015), as carbonaceous and silicate grains may align with the Galactic magnetic field with different efficiencies. More realistic simulations could be derived from three-dimensional realizations of the Galaxy's magnetic field and source distributions.

ACKNOWLEDGEMENTS

BT acknowledges the support of an STFC studentship; JD and DA acknowledge the support of ERC grant 259505. DA acknowledges support from BIPAC. We acknowledge use of the *WMAP* public maps on LAMBDA, the *Planck* public maps on the Planck Legacy Archive, the HEALPIX software and analysis package (Górski et al. 2005), and the Planck Sky Model code (Delabrouille et al. 2013).

[4] These values were found as the standard deviation of the maximum-likelihood values of r found in the different simulations.

REFERENCES

Ali-Haimoud Y., Hirata C. M., Dickinson C., 2009, MNRAS, 395, 1055
Alonso D., Dunkley J., Naess S., Thorne B., 2017, Phys. Rev. D, 95, 043504
Baumann D. et al., 2009, in Dodelson S. et al., eds, AIP Conf. Proc. Vol. 1141, CMB Polarization Workshop: Theory and Foregrounds: CMBPol Mission Concept Study. Am. Inst. Phys., New York, p. 10
Beck M. C., Beck A. M., Beck R., Dolag K., Strong A. W., Nielaba P., 2016, J. Cosmol. Astropart. Phys., 05, 056
Bennett C. L. et al., 2013, ApJS, 208, 20
BICEP2/Keck Collaboration et al., 2015, Phys. Rev. Lett., 114, 101301
Chon G., Challinor A., Prunet S., Hivon E., Szapudi I., 2004, MNRAS, 350, 914
de Oliveira-Costa A., Kogut A., Devlin M., Netterfield C., Page L., Wollack E., 1997, ApJ, 482, L17
de Oliveira-Costa A., Tegmark M., Gaensler B. M., Jonas J., Landecker T. L., Reich P., 2008, MNRAS, 388, 247
Delabrouille J. et al., 2013, A&A, 553, A96
Dickinson C., Peel M., Vidal M., 2011, MNRAS, 418, L35
Draine B. T., 2011, Physics of the Interstellar and Intergalactic Medium. Princeton University Press, Princeton, NJ
Draine B. T., Lazarian A., 1998, ApJ, 508, 157
Draine B. T., Lazarian A., 1999, ApJ, 512, 740
Fauvet L. et al., 2011, A&A, 526, A145
Fauvet L., Macías-Pérez J. F., Désert F. X., 2012, Astropart. Phys., 36, 57
Finkbeiner D. P., Davis M., Schlegel D. J., 1999, ApJ, 524, 867
Fraisse A. A. et al., 2009, in Dodelson S. et al., eds, AIP Conf. Ser. Vol. 1141, CMB Polarization Workshop: Theory and Foregrounds: CMBPol Mission Concept Study. p. 265
Fuskeland U., Wehus I. K., Eriksen H. K., Næss S. K., 2014, ApJ, 790, 104
Génova-Santos R. et al., 2017, MNRAS, 464, 4107
Giardino G., Banday A. J., Fosalba P., Górski K. M., Jonas J. L., O'Mullane W., Tauber J., 2001, A&A, 371, 708
Gold B. et al., 2011, ApJS, 192, 15
Górski K. M., Hivon E., Banday A. J., Wandelt B. D., Hansen F. K., Reinecke M., Bartelmann M., 2005, ApJ, 622, 759
Haslam C. G. T., Klein U., Salter C. J., Stoffel H., Wilson W. E., Cleary M. N., Cooke D. J., Thomasson P., 1981, A&AS, 100, 209
Haslam C. G. T., Stoffel H., Salter C. J., Wilson W. E., 1982, A&AS, 47, 1
Hensley B. S., Draine B. T., Meisner A. M., 2016, ApJ, 827, 45
Hervías-Caimapo C., Bonaldi A., Brown M. L., 2016, MNRAS, 462, 2063
Hinshaw G. et al., 2007, ApJS, 170, 288
Hinshaw G. et al., 2013, ApJS, 208, 19
Hoang T., Lazarian A., Draine B. T., 2011, ApJ, 741, 87
Ichiki K., 2014, Prog. Theor. Exp. Phys., 2014, 1
Jansson R., Farrar G. R., 2012, ApJ, 757, 14
Kayo I., Taruya A., Suto Y., 2001, ApJ, 561, 22
Kogut A., 2012, ApJ, 753, 110
Kogut A. et al., 2007, ApJ, 665, 355
Leitch E., Readhead A., Pearson T., Myers S., 1997, ApJ, 486, L23
Lewis A., Challinor A., Lasenby A., 2000, ApJ, 538, 473
Macellari N., Pierpaoli E., Dickinson C., Vaillancourt J. E., 2011, MNRAS, 418, 888
Matsumura T. et al., 2014, J. Low Temp. Phys., 176, 733
Matsumura T. et al., 2016, J. Low Temp. Phys., 184, 824
Meisner A. M., Finkbeiner D. P., 2015, ApJ, 798, 88
Miville-Deschenes M. A., Ysard N., Lavabre A., Ponthieu N., Macias-Perez J. F., Aumont J., Bernard J. P., 2008, A&A, 490, 1093
Næss S. K., Louis T., 2013, J. Cosmol. Astropart. Phys., 9, 001
Orlando E., Strong A., 2013, MNRAS, 436, 2127
Planck Collaboration XXII, 2015, A&A, 576, A107
Planck Collaboration I, 2016a, A&A, 594, A1
Planck Collaboration X, 2016b, A&A, 594, A10
Planck Collaboration XIII, 2016c, A&A, 594, A13
Planck Collaboration XLVI, 2016d, A&A, 596, A107
Planck Collaboration L, 2017, A&A, 599, A51
Poh J., Dodelson S., 2016, preprint (arXiv:1606.08922)

Downloaded from https://academic.oup.com/mnras/article/469/3/2821/3752444 by Princeton University user on 16 July 2024

Remazeilles M., Dickinson C., Banday A. J., Bigot-Sazy M. A., Ghosh T., 2015, MNRAS, 451, 4
Remazeilles M., Dickinson C., Eriksen H. K. K., Wehus I. K., 2016, MNRAS, 458, 2032
Ruud T. M. et al., 2015, ApJ, 811, 89
Rybicki G. B., Lightman A. P., 1979, Radiative Processes in Astrophysics, Wiley-Interscience, NY, 393 p
Santos M. G., Cooray A., Knox L., 2005, ApJ, 625, 575
Silsbee K., Ali-Haïmoud Y., Hirata C. M., 2011, MNRAS, 411, 2750
Stevenson M. A., 2014, ApJ, 781, 113
Tegmark M., 1998, ApJ, 502, 1
Vansyngel F. et al., 2016, preprint (arXiv:1611.02577)
Waelkens A., Jaffe T., Reinecke M., Kitaura F. S., Enßlin T. A., 2009, A&A, 495, 697
Zheng H., Tegmark M., Dillon J., Liu A., Neben A., Jonas J., Reich P., Reich W., 2017, MNRAS, 464, 3486

This paper has been typeset from a TEX/LATEX file prepared by the author.

Downloaded from https://academic.oup.com/mnras/article/469/3/2821/3752444 by Princeton University user on 16 July 2024